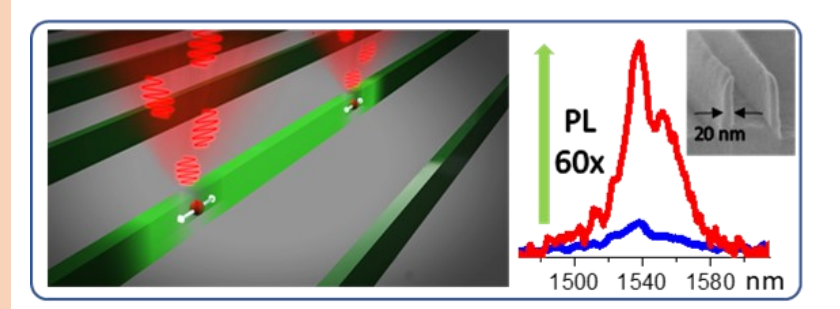
Engineered Telecom Emission and Controlled Positioning of ${\rm Er^{3+}}$ Enabled by SiC Nanophotonic Structures

Natasha Tabassum,^a Vasileios Nikas,^a Alex E. Kaloyeros, ^a Vidya Kaushik,^a Edward Crawford,^b Mengbing Huang,^a and Spyros Gallis^{a*}

- ^a College of Nanoscale Science and Engineering, SUNY Polytechnic Institute (SUNY Poly), Albany, New York 12203, USA
- b GLOBALFOUNDRIES Corp., East Fishkill, New York12533, USA



Scalable silicon carbide nanowire-based photonic crystal structures enable strong coupling and on-demand placement of rare-earth erbium ions in the nanostructures, which demonstrate substantial enhancement of the erbium technologically important 1540 nm emission.

Spyros Gallis, https://sunypoly.edu/faculty-and-staff/spyros-gallis-spyridon-galis.html

^{*} Corresponding Author

Engineered Telecom Emission and Controlled Positioning of Er³⁺ Enabled by SiC Nanophotonic Structures

Natasha Tabassum,¹ Vasileios Nikas,¹ Alex E. Kaloyeros,¹ Vidya Kaushik,¹ Edward Crawford,² Mengbing Huang,¹ and Spyros Gallis¹(☒)

- ¹ College of Nanoscale Science and Engineering, SUNY Polytechnic Institute (SUNY Poly), Albany, New York 12203, USA
- ² GLOBALFOUNDRIES Corp., East Fishkill, New York 12533, USA

ABSTRACT

High precision placement of rare-earth ions in scalable silicon-based nanostructured materials exhibiting high photoluminescence (PL) emission, photostable and polarized emission, and near-radiative-limited excited state lifetimes can serve as critical building blocks towards the practical implementation of devices in the emerging fields of nanophotonics and quantum photonics. Introduced herein are optical nanostructures composed of arrays of ultrathin silicon carbide (SiC) nanowires (NW) that constitute scalable one-dimensional nanowire-based photonic crystal (NW-PC) structures. The latter are based on a novel, fab-friendly, nanofabrication process. The NW arrays are grown in a self-aligned manner through chemical-vapor-deposition. They exhibit a reduction in defect density as determined by low temperature time-resolved PL measurements. Additionally, the NW-PC structures enable the positioning of erbium (Er³⁺) ions with an accuracy of 10 nm, an improvement on the current state-of-the-art ion implantation processes, and allow strong coupling of Er3+ ions in NW-PC. The NW-PC structure is pivotal in engineering the Er³⁺-induced 1540 nm emission, which is the telecommunication wavelength used in optical fibers. An approximately 60-fold increase of the room-temperature Er³⁺ PL emission is observed in the NW-PC compared to its thin-film analog in the linear pumping regime. Furthermore, 22 times increase of the Er3+ PL intensity per number of exited Er ions in NW-PC was observed at saturation, while using 20 times lower pumping power. The NW-PC structures demonstrate broadband and efficient excitation characteristics for Er³⁺, with an absorption cross-section (~2×10⁻¹⁸ cm²) two-order larger than typical benchmark values for direct absorption in rare-earth-doped quantum materials. Experimental and simulation results show that the Er3+ PL is photostable at high pumping power and polarized in NW-PC and is modulated with NW-PC lattice periodicity. The observed characteristics from these technologically friendly nanophotonic structures provide a promising route to the development of scalable nanophotonics and formation of single-photon emitters in the telecom optical wavelength band.

KEYWORDS

Scalable semiconductor nanowires, silicon carbide, rare-earth doped materials, erbium, photonic crystal nanostructures, on-demand positioning of emitters, telecom nanophotonics, quantum sources, long-distance quantum networks

1. Introduction

In recent years there has been a tremendous interest in the synthesis, properties, and applications of semiconductor nanowires (NWs). This interest has been complemented by the industry's enthusiasm towards faster nanodevices exhibiting high functionality with reduced energy consumption. The synthesis and simultaneous on-demand-positioning of NWs coupled with the ability to control their orientation and spatial assembly are critical factors towards the production of nanosystems and nanodevices [1]. The primary limiting challenge commonly faced, especially for feature sizes below 100 nm and bottom-up approaches, is the required deterministic and scalable integration, which involves control over the density, orientation, and spacing of the synthesized nanowires. It has been a consensus that semiconductor NWs can help cultivate the next generation of electronics and photonics [2, 3], biological and medical technologies [4,5], as well as energy technologies [6, 7]. Following this trend, a significant effort has been focused on the development of nanostructured materials that can be employed ubiquitously in several exciting emerging quantum technologies, spanning quantum sensing, quantum photonics, and quantum communication and storage [8, 9].

Macroscopic rare-earth-doped materials are one of the most

promising candidates for quantum storage of single photons and signal processing [10, 11, 12]. The realization of scalable onchip optical quantum memory and quantum optical signal processing devices requires novel nanostructured materials that must be highly integrable and compatible with existing electronic circuits, waveguide architectures, and current chipscale and silicon (Si) process technology [2, 13]. The controlled placement of rare-earth ions into Si-based wide bandgap nanostructured materials with high integration functionality, such as silicon carbide (SiC) NWs [9, 14, 15, 16], can serve as critical building-blocks towards the implementation of such quantum devices. Silicon carbide is a silicon-based wide bandgap material with excellent thermal, mechanical and physical properties. SiC is chemically inert and exhibits almost negligible magnetic moment (a necessary requirement for hosting quantum emitters)[17], making it a promising host material for single-photon emitters and qubits with several applications in quantum technologies [9]. Rare-earth erbium (Er3+) ions have an emission at the technologically important wavelength of \sim 1540 nm, as it falls in the lowest loss wavelength range (telecom Cband) of fiber optics networks [18]. As such, Er-doped materials, are the only materials that can potentially meet the current requirements to realize a quantum memory/repeater at telecom C-band wavelengths [11, 12].

For optical quantum storage and signal processing

applications, optically active rare-earth ions in solid-state hosts must exhibit high optical pumping and photoluminescence (PL) emission to enable efficient storage and high-fidelity optical readout of the ion's quantum state. Furthermore, long nearradiative-limited excited state lifetimes of the ions are important to achieve long storage and coherence times [10, 11]. To this end, photonic crystal (PC) nanostructures, and PC cavities have attracted attention for their ability to suppress or enhance spontaneous emission rate, respectively, and control light directionality of emitters [19,20]. By properly engineering such nanophotonic structures, it is possible to suppress (photonic bandgap structures) or enhance (photonic cavities) the local density of photon states (LDOS) compared to the free-space value, thus respectively, decreasing or increasing the emission rate. This has been recently demonstrated for rare-earth neodymium- and erbium-based quantum sources and memories [13,21]. Such nanostructures are typically fabricated via top down approaches, such as electron beam lithography (as is the case in [21]) or focused ion beam [9], or bottom-up approaches, such as the vapor-liquid-solid [22]. However, these approaches suffer from drawbacks; top-down fabrication of features below 30 nm features becomes difficult and costly, while bottom-up approaches must facilitate the required control over density, geometry, orientation, spacing, and alignment of individual structures [23]. Realization of PC nanostructures requires the development of advanced synthesis methods and novel nanofabrication schemes [9].

In this paper, we report on a new class of CMOS-compatible nanophotonic structures based on scalable SiC nanowire-based photonic crystals (NW-PC) doped with and without oxygen, and Er ions. The ultrathin NWs were fabricated in a self-aligned manner through a novel catalyst-free chemical-vapordeposition (CVD) synthesis route, without the use of a lithographic-pattern-transfer technique. This nanofabrication scheme reduces defect density and enables precise control over the geometry of the NWs. The surface roughness and crystallinity of the NWs enables the growth of ultrathin ≤20 nm structures and enables the controlled placement of Er³⁺ ions down to a nanoscale resolution. Another major advantage is the engineering of the Er3+-induced 1540 nm emission through efficient coupling with the NW-PC. We demonstrate that these one-dimensional (1D) photonic crystal (PC) structures provide an extremely efficient excitation route for Er3+, exhibiting a photostable and polarized Er3+ emission for potential applications in nanophotonics, and long-distance telecom optical quantum networks.

2. NANOFABRICATION

2.1 Fabrication of self-aligned ultrathin NW arrays

Self-aligned 1D NW arrays grown at predetermined positions were fabricated on silicon substrates via thermal CVD. An abridged fabrication process of the NW-PC is schematically depicted in Figure 1. First a hydrogen silsesquioxane (HSQ) negative-tone resist layer was spin-coated onto Si. We used electron beam lithography to expose line patterns, and the resulting wafer piece was developed in a chemical solution bath yielding an HSQ ribbon array (Figure 1a-i) [24]. After the

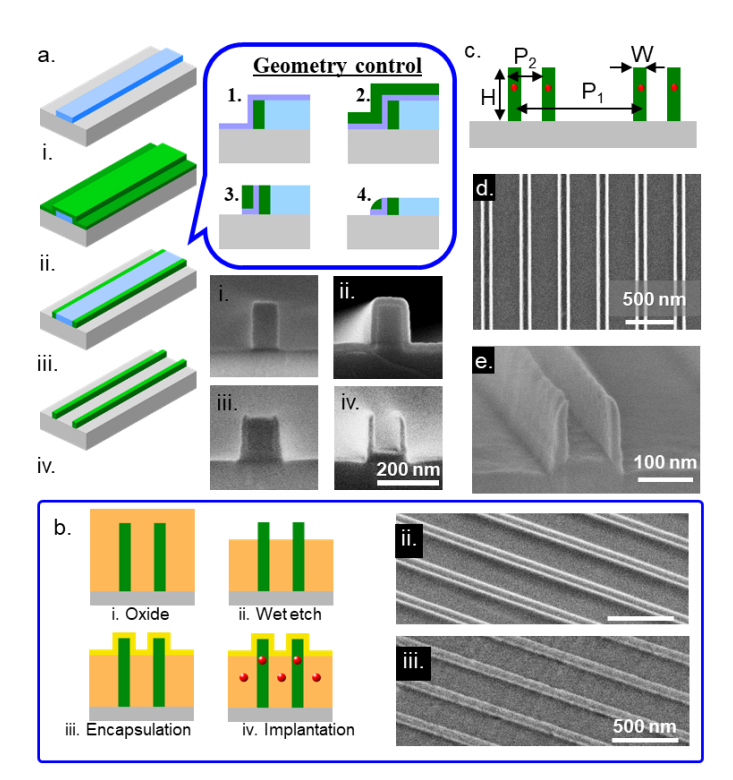


Figure 1. SiC nanostructured materials through on-demand placement of NW and Er3+. (a) Fabrication process steps for realizing self-aligned 20 nm-width NW-PC structures and representative crosssection scanning electron microscopy (SEM) images. i. Spin-coating and electron beam lithography of HSQ (blue) to create a ribbon template on a substrate (gray); ii. Self-aligned deposition of conformal SiC or SiC:0 ultrathin layer (green). Geometry control using a conformal oxide (purple) and SiC layer; iii. Anisotropic RIE; iv. Wet-etch removal of HSQ. (b) Ondemand integration of Er ions in the NW-PC. i. Deposition of sacrificial oxide layer (orange) and CMP; ii. Combination of RIE and wet-etch to expose the top of NWs; iii. Deposition of thin oxide layer (yellow) based on targeted ion implantation depth. The corresponding top-down SEM images of step ii & iii are shown; iv. Er ions (red circles) implantation and wet-etch to remove oxide layers. (c) Schematic cross-section diagram of the resulting Er-doped 1D NW-PC structures with lattice periodicity P₁. P₂: Sub-lattice periodicity; H: Height of the NWs; and W: width of the NWs. (d) Low magnification top-down and (e) High magnification cross-section SEM images of the resulting Er-doped NW-PC structures (W= 20 nm, P₁= 400 nm, P₂= 100 nm, H= 130 nm).

development process, we conformally deposited ≤ 20 nm-thick SiC (with an index of refraction, n = 2.7) or SiC doped with oxygen, SiC:0 (SiC_{0.5}O_{0.8}, n = 2.2), onto the HSQ template using CVD processing (Figure 1a-ii), described elsewhere [25, 26].

Post-deposition thermal treatment was carried out in forming gas ambient (95% argon (Ar) and 5% hydrogen (H₂)) at 1100°C for 1 hour. Following the annealing of the ultrathin chemically grown layer, we performed anisotropic reactive ion etching (RIE) to remove the top SiC or SiC:O layer, leaving the sidewall self-aligned layer (NWs) intact and exposing the HSQ template (Figure 1a-iii). For control over the geometry of the NWs, the SiC sidewalls are encapsulated with a conformal oxide and SiC layer. This helps protect the self-aligned sidewalls during the ensuing RIE and enables control over shape and height of the resulting NWs. A wet etch, buffered hydrofluoric acid (BHF), was used to remove the HSQ, yielding ultrathin NW arrays synthesized in a self-aligned manner (Figure 1a-iv).

This synthesis route utilizes new precursor chemistry, TSCH (1,3,5-trisilacyclohexane) from Gelest Inc. (see Methods), resulting in highly crystalline matrix with good surface roughness, enabling the fabrication of NWs with width (W) of 10nm (examples of more structures are shown in Figure S1). The critical dimension, width, of the NWs solely depends on the thickness of the conformal sidewall layer. The height (H), lattice periodicity (P_1) , and sub-lattice periodicity (P_2) of the NW array are also shown in Figure 1c.

2.2 On-demand placement and integration of Er^{3+} into NW-PC

Panel b of Figure 1 presents the major process steps employed to engineer the position of Er³+ ions in the NW-PC. First, we deposited a sacrificial thick oxide layer onto the NW array using CVD [24] followed by chemical mechanical planarization (CMP) to flatten and thin the oxide layer. We then performed controlled RIE and wet-etch steps to recess the oxide layer and to expose the top of the NWs. A thin (15 nm) conformal CVD-grown oxide layer was then deposited to encapsulate the NWs. We can modulate the thickness of the oxide layer based on the targeted ion-implantation depth in the NWs. Accordingly, the remaining thicker oxide layer between the NWs prevents ion implantation into the substrate.

Samples were then subjected to a 150 keV beam of erbium ions targeting ions to be embedded into 30 nm depth from the top of the NW arrays, as determined by Transport of Ions in Matter (TRIM) simulations. Various doses of Er ions – 1×10¹³ cm⁻² (low), 5×10^{13} cm⁻² (medium) and 1×10^{14} cm⁻² (high) were implanted into the NW-PC structures and (thin film) samples by ion implantation. We then carried out a wet-etch to remove the oxide layers yielding the controlled-Er-doped NW-PC structures (Figure 1d-e). This process was followed by a post-implantation Ar annealing (1 hour, 900°C) and a forming gas (95% nitrogen (N2) and 5% H2) thermal treatment (1 hour, 850°C) to activate the Er ions optically and for surface passivation [27]. The integration scheme dictates the final positions of the implanted ions to be within the 10 nm width of the NWs, which is an improvement to the accuracy of a state-of-the-art deterministic ion implantation process for single atom devices in [28] and the single ion implantation process in [29].

3. RESULTS AND DISCUSSION

3.1 Modeling of a dipole emission in NW-PC structures

The extraction efficiency of the spontaneous emission from a dipole in 1D NW-PC and a uniform slab without a PC structure was explored using finite-difference time-domain (FDTD) calculations (Figure 2). We used a monitor parallel to the *xy*-plane to calculate the extraction efficiency of the emitted radiation power from the dipole (see Methods and Figure 2a). The extraction efficiency, n_{ext} , is defined as the fraction of the radiation power transmitted through the monitor to the total emitted power from the dipole [19, 30].

FDTD calculations revealed that the emission extraction efficiency from the SiC slab was ~3.6% at most wavelengths across the simulated range (Figure 2b). The observed behavior

is consistent with findings from other studies indicating a high density of guided optical modes within the high-refractive-index SiC over a broad wavelength range [19, 30]. Similarly, we performed FDTD calculations in SiC NW-PC structures with three different P_1 values that revealed two major differences. First, the extraction efficiency was enhanced throughout the whole investigated wavelength range with values up to $\sim 40\%$ (Figure 2b). Specifically, in the 600-nm- P_1 NW-PC sample, the Er³+-induced 1540-nm emission extraction efficiency was 39%, an order of magnitude higher than that in the slab with $\sim 3.6\%$. Second, a modulation of the extraction efficiency was observed with NW periodicity P_1 as shown in Figure 2b. For example, at 1000 nm, n_{ext} . from the 200-nm and 600-nm- P_1 SiC NW-PC structures are 24% and 37%, respectively. Similar trends were also observed in SiC:O systems (Figure 2b, grey data points).

The extraction efficiency enhancement of the dipole's spontaneous emission in NW-PC structures is expected because of the suppression of in-plane emission modes (guided modes). By eliminating guided modes at transition frequencies, spontaneous emission can be coupled efficiently to free space vertical modes, resulting in substantially enhanced extraction efficiency [19, 30]. Therefore, radiation originating from NW-PC structures results in enhanced light emission in the vertical direction. This behavior is supported by our spatial distribution calculation of the extracted power radiation ($\sim |E|^2$) at 1540 nm (Figure 2c). In the case of the thin-film slab, a significant portion of the radiation is confined within the slab (x-direction in this simulation) (Figure 2c-i). Conversely in NW-PC, guided modes

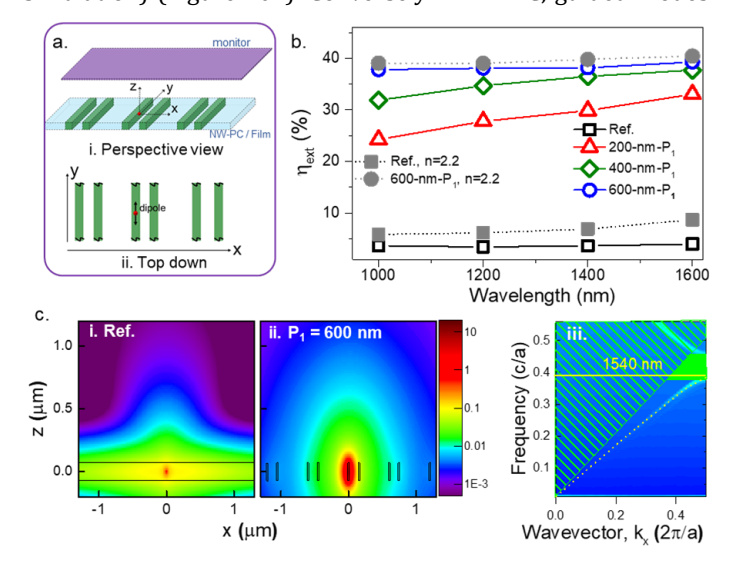


Figure 2. FDTD modeling of the spontaneous emission extraction efficiency for the NW-PC and reference (Ref.) thin-film slabs. (a) i. Schematic diagram of the geometry used in the FDTD computation with the relative position of the monitor used for extraction efficiency calculation. ii. Top-down schematic of the geometry showing the orientation of *y*-polarized dipole. (b) The emission extraction efficiencies, $\eta_{\rm ext}$ from the NW-PC structures and reference as a function of wavelength. Grey data points refer to SiC:O structure with n = 2.2. (c) Calculated spatial distribution of the electric field, $|E|^2$, at 1540 nm in the zx plane (y-polarized dipole, n = 2.7) for i. the reference and ii. the 600-nm-P₁ NW-PC. The dashed lines in each map represent the outline of the structure. iii. Dispersion relation of the 600-nm-P₁ NW-PC structure (periodicity, a = P₁ = 600 nm), showing an incomplete photonic bandgap extending from 190 THz (1577 nm) to 229.2 THz (1308 nm).

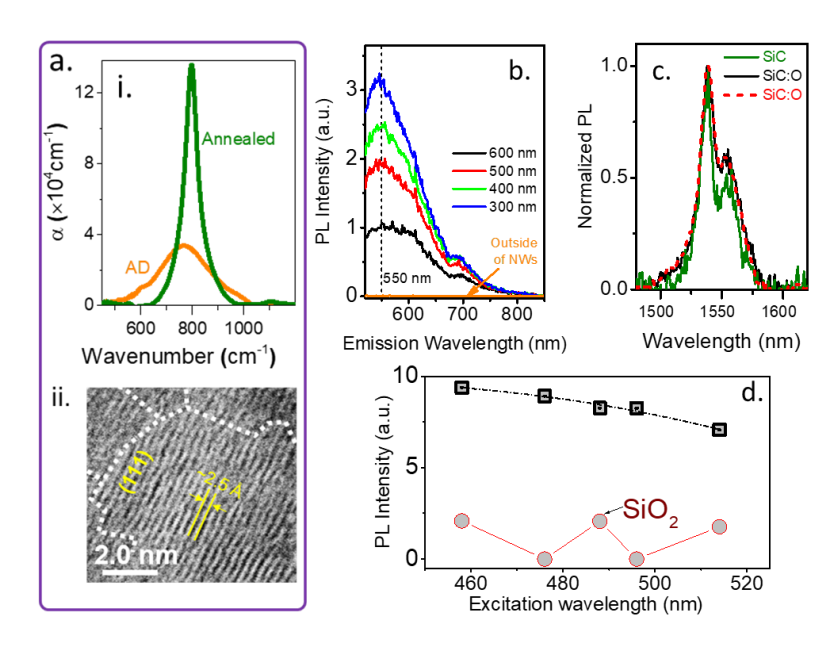


Figure 3. Structural and PL properties. (a) i. FTIR absorption spectra of the Si-C stretching mode for the as-deposited (AD) and 1100° C-annealed 20 nm thin-films showing the transformation from amorphous to polycrystalline phase. ii. Representative HR-TEM image of annealed NW-PC showing average grain size of ~5 nm with 3C-SiC crystalline phase. (b) Visible PL spectra from NW-PC structures under 476 nm laser excitation. PL of the same wavelength range from outside of the nanowires is shown in orange. (c) Characteristic room-temperature Er^{3+} emissions at ~1540 nm and ~1555 nm in NW-PC structures under 488 nm (solid lines) and 476 nm (dotted line) excitations. (d) Photoluminescence excitation (PLE) spectra at 1540 nm emission from NW-PC (square) and SiO_2 (circle symbols) under a range of laser excitation wavelengths from 458 nm to 514 nm. Error bars are not depicted as the errors are smaller than the symbol size.

are eliminated as it is presented in Figure 2c-ii and Figure S2 (Supplementary Material). For the 600-nm-P₁ structures, 1540 nm emission is inhibited along the *x*-direction more prominently than other NW-PC structures, as the 1540 nm wavelength falls within the computed incomplete photonic bandgap of the structure (Figure 2c-iii). Only the 600-nm-P1 structures among our fabricated arrays exhibited a photonic bandgap containing 1540 nm. Nevertheless, due to the ultrathin geometry of nanostructures the extraction efficiency is enhanced due to lack of total internal reflection even if there is no bandgap present containing the frequency of interest [19].

3.2 Morphological and structural properties of materials

Fourier transform infrared (FTIR) spectroscopy measurements showed complete crystallization of the as-deposited amorphous SiC materials at temperatures ≥1000°C, in accordance with our previously reported results (Figure 3a-i) [31]. In this respect, the line shape of the Si-C stretching mode (~800 cm⁻¹) of the asdeposited material transformed from Gaussian to Lorentzian after annealing at 1100°C, which was accompanied by a substantial narrowing of the full width at half maximum (FWHM) (~30 cm⁻¹), comparable to values for high-quality crystal SiC [32]. The surface roughness of as-deposited and annealed materials were analyzed by atomic force microscopy. Both materials have extremely flat surfaces with a mean surface roughness of 1-2 Å (measured from several 1 μm² areas). X-ray diffraction (XRD), and high-resolution transmission electron microscope (HR-TEM) analyses agreed with the FTIR results, revealing the formation of cubic 3C-SiC. The NWs were polycrystalline with average nanocrystal grain size of ~5 nm as

presented in Figure 3a-ii.

3.3 Er³⁺ PL properties in SiC NW-PC structures

We investigated the room-temperature (RT) visible and Er3+ emission properties of undoped and Er-doped NW-PC structures, respectively, by PL spectroscopy using a micro-PL (µPL) system (Figure S3 in Supplementary Material) at different laser visible excitation wavelengths (e.g. 458 nm, 476 nm, 488 nm, 514.5 nm). Figure 3b shows the matrix-related PL emission spectra of undoped NW-PC structures, with a peak PL emission at ~550 nm in concurrence with our previous studies [24,25]. Pertaining to Er3+ emission, the 476 nm excitation is nonresonant excitation while the 488 nm excitation corresponds to resonant transitions from the ground state ${}^4I_{15/2}$ to the ${}^4F_{7/2}$ excited state in Er3+. The characteristic Er3+ emission, due to intra-4f transitions ${}^{4}I_{13/2} \rightarrow {}^{4}I_{15/2}$, [18] at ~1540 nm and ~1555 nm were observed in both SiC and SiC:O NW-PC as shown in Figure 3c (Er dose: 1014 cm-2). Er3+-1540 nm PL emission was observed using various visible pumping wavelengths in NW-PCs, demonstrating the structures' broadband excitation characteristics (Figure 3d). Conversely, for the SiO₂:Er system, only resonant transitions [33] to the excited states of Er3+ occurred around the excitation wavelengths of 458 nm, 488 nm and 514.5 nm in agreement with other reports [34, 35].

NW-PC structures with larger P_1 periodicity, resulting in a lower density of NWs, would be expected to have lower visible PL due to their volumetric difference and also lower Er^{3+} -1540 nm PL due to the corresponding decreased number of total Er^{3+} ions in the NW-PC. This volumetric effect was observed in the visible PL emission at 550 nm, where PL decreased for increasing P_1 periodicity (Figure 4a). However, the opposite trend was observed for the Er^{3+} PL. The structures with the

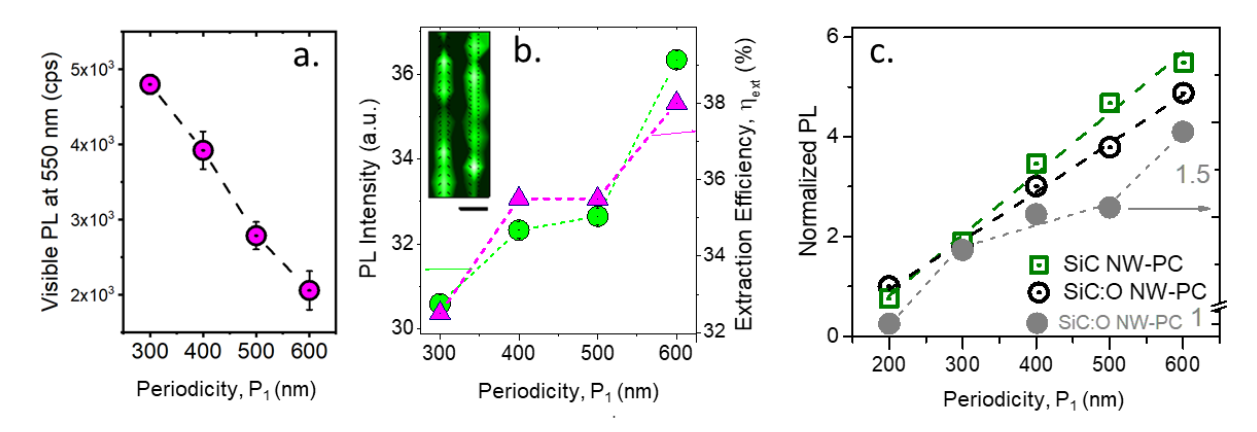


Figure 4. Volumetric effects on PL properties of NWs. (a) PL intensity (counts per second -cps) at 550 nm as a function of P_1 periodicity .(b) Measured PL intensity at 1540 nm (green circle) and FDTD-computed extraction efficiency (pink triangle) for different NW-PC structures. Error bars are not depicted as the errors are smaller than the symbol size. Inset: PL intensity mapping of NW-PC with $P_2 \times P_1 = 150 \times 600$. The scale bar is 500 nm. (c) Er³⁺ PL intensity in SiC NW-PC and SiC:0 NW-PC as a function of P_1 ; the difference of implanted Er ions was accounted for among the NW-PC. Three different NW-PC structures were measured for each P_1 . The grey data points represent the Er³⁺PL in SiC:0 NW-PC without the volumetric normalization.

smallest periodicity, $P_1 = 200$ nm, exhibited the lowest Er^{3+} PL among the studied NW-PC structures (Figure 4b). After accounting for the decrease in the number of Er^{3+} ions in the air region of the different NW-PC structures (Section S4 and S5 for more details), the Er^{3+} PL increases in a monotonic fashion by a factor of about five as P_1 increases from 200 to 600 nm (Figure 4c). Furthermore, the modulation of the Er^{3+} PL with P_1 periodicity presented a direct correlation with the FDTD-computed extraction efficiency in NW-PC (Figure 4b). This correlation was observed for equivalent SiC and SiC:0 NW-PC structures, and we observed the highest Er^{3+} PL intensity in the 600-nm- P_1 SiC:0 structures.

To further our understanding of the NW-PC effect on Er3+ emission, we studied a representative 600-nm-P₁ SiC:O NW-PC devices (Er dose: 1013 cm-2). It is worth highlighting that, with the experimental μPL setup used in this study, the Er³⁺ PL emission was not detected from the thin film without a PC structure (Ref.) at pumping power densities below 40 kW/cm². This power value can be defined as the threshold power for detecting Er³⁺ PL from the thin film. In contrast, Er³⁺ PL from the 600-nm-P₁ NW-PC was measurable with a pumping power as low as 0.9 kW/cm². This behavior suggests that collectively the pumping and emission-extraction efficiencies of Er³⁺ in NW-PC are higher compared to their thin-film analog. At the threshold power, and accounting for the same number of Er ions (Supplementary Material), the Er3+ PL collected from the 600nm-P₁ NW-PC was found to be approximately 60 times higher than thin-film (Figure 5a). Moreover, the PL intensity ratio between the NW-PC and thin-film samples increases monotonically with decreasing Er dose. For example, the PL ratio was approximately 17 and 35 for, respectively, the 1014 cm⁻¹ ² and 5×10¹³ cm⁻² doses (inset in Figure 5a). Time-resolved photoluminescence (TRPL) of the 1540 nm emission revealed a luminescence lifetime, τ , of ~2.7 ms in 600-nm-P₁ NW-PC structures.

To obtain more insight into these compelling Er^{3+} PL behaviors in the NW-PC we measured the Er^{3+} PL emission as a function of excitation power (Figure 5b and Figure S6). After subtracting the linear background and the detector dark counts, we fitted the 1540 nm-emission data to the following equation [15, 35],

$$I(P) = \frac{I_{sat}}{1 + \frac{P_{sat}}{P}} \tag{1}$$

where I(P) is the Er³⁺ PL intensity at a given excitation power P, I_{sat} is the saturation intensity and P_{sat} is the excitation power required to yield half of I_{sat} . Figure 5b-i presents the results from a representative 600-nm-P₁ NW-PC nanostructure, revealing I_{sat} = 4244 ±114 cps and P_{sat} = ~8.3 kW/cm². I_{sat} and P_{sat} were also extracted for a representative thin-film sample, giving I_{sat} = 192 ± 10 cps and P_{sat} = ~150 kW/cm² (Figure 5b-ii). These values indicate an approximate 20-fold increase in both pumping efficiency and Er³⁺ emission output flux (I_{sat}) in NW-PC. Furthermore, equation (1) can be expressed as a function of the photon flux of incoming photons, φ , by [18, 36],

$$I = \frac{I_{sat}}{1 + \frac{1}{\sigma \varphi \tau}},$$
(2)

where σ is the effective excitation cross-section and τ is the luminescence lifetime that was experimentally determined in TRPL. $I_{\rm sat}$ is given by $I_{\rm sat} = N^*/\tau_r$, where τ_r and N^* are, respectively, the radiative lifetime and the concentration of the optically active erbium ions. We then fitted the experimental power-dependence data to Eq. (2) using the observed Er PL lifetime, which yielded an effective cross-section value of $2.2\times10^{-18}\,\rm cm^{-2}$ for the NW-PC. This value is one order larger than that of the thin-film sample ($2.8\times10^{-19}\,\rm cm^{-2}$), and two orders of magnitude higher than the typical range of $\sim10^{-20}$ - $10^{-21}\,\rm cm^2$ for Er-doped materials [37, 38].

The matrix-related PL spectrum of the NW-PC devices is characterized by a broadband luminescence feature in the spectral range of 500 – 750 nm, with the dominant PL occurring around 550 nm wavelength. To this end, some of the Er³+ transitions , such as $^4I_{15/2} \rightarrow ^2H_{11/2}$ (514 - 520 nm), $^4I_{15/2} \rightarrow ^4S_{3/2}$ (550 nm), and $^4I_{15/2} \rightarrow ^4F_{9/2}$ (660 nm), are in resonance with the broadband PL of the NW-PC devices [33]. The PL and PLE data, thus, demonstrate an efficient energy transfer mechanism between the nanostructured matrix and Er³+ ions, as the Er emission can be sensitized by the nanostructured matrix. Effective light-trapping by multiple scattering events can also

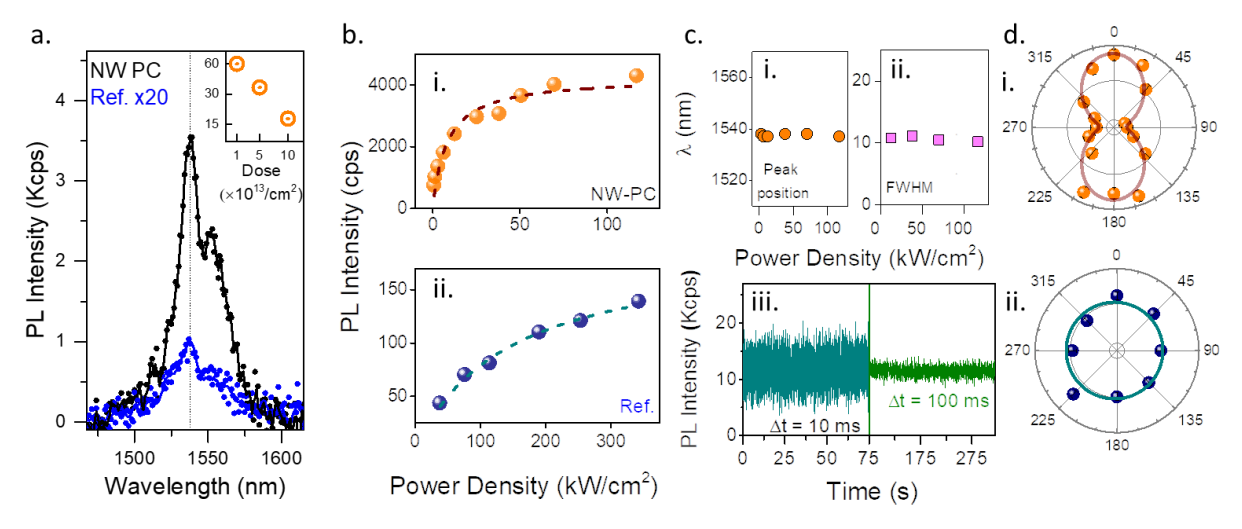


Figure 5. Comparison of 1540 nm emission characteristics between Er^{3+} in 600-nm- P_1 NW-PC and thin-film. Photostability of Er^{3+} emission in 600-nm- P_1 NW-PC. (a) Room-temperature steady-state Er^{3+} PL spectra in 600-nm- P_1 NW-PC and thin-film (Ref.) under 488 nm excitation (Pumping power density: 40 kW/cm²; Er dose: 1×10^{13} cm⁻²; the difference of implanted Er ions was accounted for between the NW-PC and thin-film). The Er^{3+} PL intensity in thin-film was multiplied by 20 for presentation purposes. Inset: Ratio of Er^{3+} PL intensity between NW-PC and thin-film as a function of Er^{3+} PL emission peak intensity as a function of pumping power density from i. 600-nm- Er^{3+} PL emission peak intensity as a function of pumping power density from i. 600-nm- Er^{3+} PL spectra as a function of pumping power. iii. Er^{3+} PL time traces with sampling bins of Er^{3+} PL material Er^{3+} PL time traces with sampling bins of Er^{3+} PL material Er^{3+} PL peak area as a function of the emission polarization from i. 600-nm- Er^{3+} NW-PC; and ii. thin-film. The polarization angle of the excitation source was kept parallel along to the NWs' length.

increase absorption probability of the incident light in the NW-PC devices [7].

Photostability under high pumping is important for photonic applications. The peak position and lineshape (FWHM) of the observed Er3+ PL emission in NW-PC remained unchanged with pumping power (Figure 5c-i,ii), showing good photostability of the Er-doped nanophotonic structures. Furthermore, we examined the photostability of Er3+ PL under high pumping power as a function of time. The Er3+ PL time-traces on two different timescales are shown in Figure 5c-iii. The Er3+ PL count-rate remained constant over several minutes with no indication of photobleaching. Furthermore, the large geometric anisotropy of the ultrathin NW also results into anisotropy of the emission and absorption properties of the emitters [39, 40]. As presented in Figure 5d-i, the Er3+-emission from NW-PC was found to be predominantly polarized along the length of the NWs, with emission polarization degree, ρ_{em} of ~0.4. Even if the dipoles in a nanowire are randomly oriented, the emitted light from the nanowire will be preferentially oriented along the nanowire axis and ρ_{em} is expressed as [41]:

$$\rho_{em} = \left| \frac{I_{\parallel} - I_{\perp}}{I_{\parallel} + I_{\perp}} \right| \tag{3}$$

where I_{\parallel} or I_{\perp} is the intensity of respectively the most (polarizer parallel to NWs) or least (polarizer perpendicular to NWs) intense PL respectively. In contrast, Er³⁺ PL emission from the thin-film appears completely isotropic (independent from emission polarization direction) (Figure 5d-ii).

3.4 Optically active Er3+ concentration calculation

and defect density

To estimate the concentration of the optically active Er^{3+} ions in the NW-PC and thin-film, we used the following approach described in more details in Section S7. In the linear pumping regime (low pumping power), where the excitation rate constant, $\sigma\varphi$ is much smaller than the de-excitation rate constant, $1/\tau$ ($\sigma\varphi\tau$ << 1), Equation (2) can be approximated by,

$$I = \frac{n_{ext} \, \sigma \varphi \tau N^*}{\tau_r} \tag{4}$$

At saturation (high pumping power), where $\sigma \phi \tau >> 1$, the PL intensity is equal to,

$$I_{sat} = \frac{n_{ext} N^*}{\tau_r}$$

As discussed, at saturation the I_{sat} ratio between the NW-PC and thin-film was ~22. We calculated the radiative lifetime $(\tau_{r,NW} = \Gamma_{r,NW}^{-1})$, reciprocal of the radiative PL decay rate Γ_r , of the NW-PC structure relative to the lifetime in the reference thin-film $(\tau_{r,ref} = \Gamma_{r,ref}^{-1})$ using FDTD simulation [30, 42]. In this respect, the total power radiated by the dipole within the NW-PC (P_{NW}) is proportional to the radiative spontaneous emission

the case of the 600-nm-P₁ NW-PC and thin-film, we calculated the emission rates ratio as
$$\frac{\Gamma_{r,NW}}{\Gamma_{r,ref}} = (\frac{\tau_{r,NW}}{\tau_{r,ref}})^{-1} = \frac{P_{NW}}{P_{ref}} \approx 0.39$$

rate $\Gamma_{r,NW}$, and equivalently for the reference thin-film. Thus, in

Using Equation (5) and the extraction efficiency ratio between the NW-PC and thin-film, as determined by FDTD computations, we estimated [43] the optically active Er^{3+} concentration in NW-PC to be \sim 12.4 times higher than that in the thin-film.

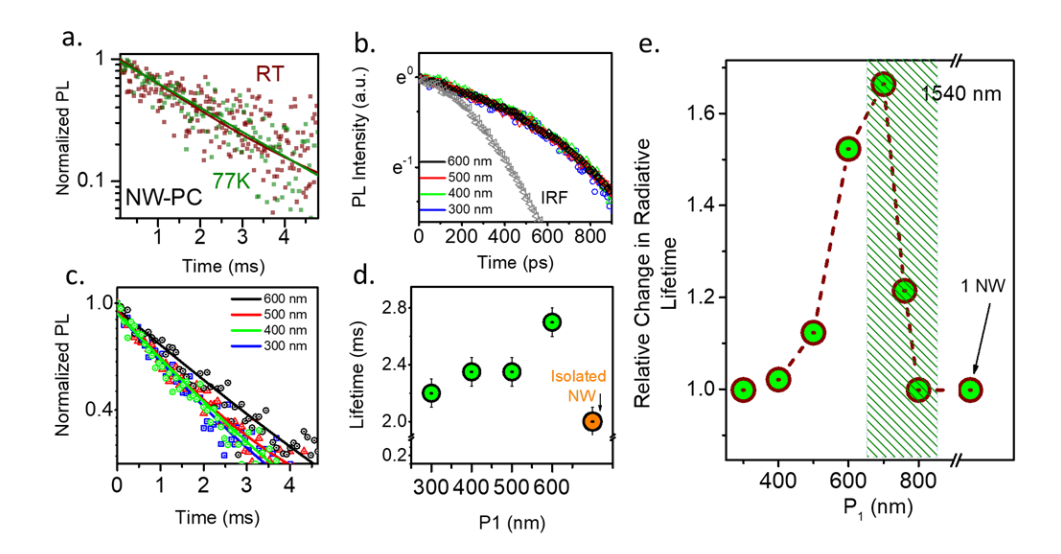


Figure 6. Effect of NW-PC structure on Er^{3+} PL emission dynamics. (a) Er^{3+} PL (~1540 nm) decay in the 600-nm- P_1 NW-PC structure under 488 nm pulsed excitation at 77 K and 300 K (red points: 300 K (RT); green points: 77 K). The Er^{3+} PL lifetime in NW-PC, as obtained from single exponential fitting, was calculated to be ~2.7 ms for both 77 K and 300 K. The solid lines indicate fits to the data. (b) PL decay of 550 nm emission from the NW-PC structures (legend: P_1) with instrument response function (IRF) in gray. (c) Room-temperature Er^{3+} PL decay at 1540 nm from different NW-PC structures (legend: P_1). Solid lines represent single exponential fits. (d) Er^{3+} PL lifetimes for the different NW-PC structures and for a single NW (orange). (e) Computed relative radiative lifetime from NW-PC with different P1 and a single NW. Data points corresponding to the NW-PC with periodicity values beyond our fabricated structures are shown under the shaded region.

Considering the decrease in the number of Er^{3+} ions in the air region for the NW-PC structures ($\sim 0.083 \times$ decrease), the total number of Er^{3+} was found to be approximately $\sim 3\%$ more in NW-PC. Nevertheless, we observed that the Er^{3+} PL was saturated at much lower power in the NW-PC structures, indicating a more efficient mechanism of pumping Er^{3+} compared to the thin-film. As mentioned in the introduction, an enhanced pumping efficiency is important for solid-state photonics, and quantum communications applications [9, 11].

The integration of rare-earth ions in wide-bandgap ultrathin NWs can offer supplemental benefits. It can be argued that Auger and energy back-transfer effects are appreciably reduced in wide-bandgap SiC and SiC:O due to low concentration of free carriers and the large mismatch between their bandgap and the first excited state of Er3+ respectively [24, 36]. Confinement effects on electron-phonon interaction may be expected primarily due to absence of low-energy acoustic phonon modes in ultrathin NWs, resulting in different luminescence dynamics of Er3+ at low temperatures [44]. Moreover, in ultrathin NWs a decreased bulk defect-density [45], and a strain-relaxed environment in the material is expected [46, 47], and hence a smaller probability of nonradiative sites within the ion's recombination volume. Thus, in ultrathin NW-PC having wellpassivated surfaces, excited Er3+ is expected to be exposed to a smaller number of bulk non-radiative recombination sites compared to its bulk analog, which can lead to an increased PL lifetime [45]. From deconvolution of the PL spectra at roomtemperature, we observed that spectral linewidth is narrower in NW-PC structures (~10 nm) compared to the thin-film sample (~18 nm), which can be due to reduction in defect density and/or reduction in the number of optically active ions.

To access the influence of non-radiative quenching processes in the NW-PC structures, we performed TRPL of the 1540 nm

emission at 77 K. As can be seen in Figure 6a, the observed Er³⁺ luminescence lifetime did not change $(2.7 \pm 0.1 \text{ ms})$ with respect to its 300 K value. The Er³⁺ PL dynamics of the NW-PC implies a good quality material, with significantly low defect density and a well-passivated surface. It may be thus inferred that the higher concentration of optically active Er3+ in NW-PC can be the result of reduction of bulk defect-density, as compared to the Er3+ PL dynamics of the thin-film (Figure S8), and more effective thermal annealing process in forming optically active Er ions due to the NW geometry. Additionally, with decreasing Er dose the number of Er³⁺ ions in NW-PC also decreases, which results in an even lower probability of a defect center being within the ions recombination volume. This may explain the trend of increased PL intensity ratio with decreasing Er dose between the NW-PC and thin-film mentioned in section 3.3 (inset of Figure 5a).

The much shorter Er^{3+} PL lifetime in thin films (Figure S8) can be attributed to an increase of nonradiative de-excitation paths for Er ions in the thin-film matrix in agreement with other reports [48,49]. Furthermore, reduction in the effective refractive index in NW-PC and confinement of the Er ions within the NW may reduce the photon density of states for emission and thereby reduce the transition rate and correspondingly increase the Er luminescence lifetime [36]. The effective refractive index in NW-PC is expected to be between that of air (n=1) and thin-film (n=2.2).

As discussed, we observed that the Er³+ PL from NW-PC was modulated with P_1 periodicity and was correlated with the computed extraction efficiency trend at 1540 nm (Figure 4b). In conjunction to the different behavior between the steady-state PL at 550 nm and 1540 nm emissions from NW-PC structures, we also observed different trends in the luminescence dynamics at these wavelengths. Average lifetime at 550 nm was found to be the same, $\sim\!680\pm40$ ps, for all the NW-PC structures (Figure

6b). However, luminescence lifetime of Er-PL at 1540 nm was found to be approximately the same, 2.3± 0.1 ms, only for NW-PCs with 300-, 400-, and 500-nm-P₁ periodicity (Figure 6c,d). For the 600-nm-P₁ NW-PC structures, in agreement with the computed radiative lifetimes (Figure 6e), we observed a longer lifetime (2.7 ± 0.1 ms), which suggests that an additional physical mechanism is contributing to the modulation besides nanostructuring and reduced defect density effects. The spontaneous emission rate of PC structures is predicted to decrease when the emission spectrum lies within the photonic bandgap [20, 30], as in the case of 600-nm-P₁ NW-PC structures, yielding longer luminescence lifetime. We observed a $\sim 15\%$ and ~30% relative difference in lifetimes from experimental (Figure 6d) and computational (Figure 6e) results, respectively, between 600-nm-P₁ and the three other NW-PC that do not have a photonic bandgap containing 1540 nm. As expected for our one-dimensional 600-nm-P₁ NW-PC structures, the increase in PL lifetime was less pronounced compared to the increase observed in two-dimensional photonic bandgap materials (~80% in Ref. 30).

The increase of the Er³+ PL lifetime in NW-PC, decrease of its PL emission rate as $\Gamma_{NW} = \tau_{NW}^{-1} = \Gamma_{r,NW} + \Gamma_{nr,NW}$, is coupled to the above mechanisms (Γ_{nr} is the nonradiative decay rate). $\Gamma_{\rm NW}$ is influenced by the complex interplay of the radiating Er³+ ($\Gamma_{r,NW} = \tau_{r,NW}^{-1}$) and its interactions with the nanophotonic structure (e.g. NW geometry, nanostructuring effect, photonic bandgap), as well as the surrounding defectivity (e.g. ion's energy transfer to competing nonradiative decay channels, $\Gamma_{nr,NW} = \tau_{nr,NW}^{-1}$).

4. Conclusions

In summary, we present a new nanofabrication scheme for the integration of rare-earth Er ions into solid-state scalable SiC nanostructures. These nanostructures encompass a new class of tailorable ultrathin photonic crystal structures, thus enabling the engineering of the spontaneous emission characteristics of Er3+. Both FDTD calculations and PL measurements revealed that the Er-induced emission efficiency can be enhanced by tailoring the geometry the NW-PC structure. We experimentally observed substantial enhancements for both the roomtemperature 1540-nm-emission and absorption cross-section in NW-PC. This holistic approach can cultivate an alternative pathway towards the development of scalable nanophotonics (e.g. integration into photonic circuity and cavity) at telecom wavelengths that could be benefited by the controlled placement of rare-earth Er3+ ions and the modification of the ion's emission in scalable SiC nanophotonic structures.

5. Methods

5.1 Synthesis of NW array structures

Silicon (100) wafers were spin-coated with HSQ negative-tone resist at 1000 rpm followed by a soft-bake, yielding an approximately 130 nm thick HSQ layer. We exposed the HSQ layer using a Vistec VB300 and a Voyager Raith electron-beam lithography tool using line patterns created in the Layout Editor. Following the exposure, development was performed in tetramethylammonium hydroxide (TMAH) yielding HSQ ribbon arrays. We conformally deposited 20 nm of SiC/ SiC:O onto the

HSQ ribbon arrays using a home-built thermal CVD system at 800° C. CVD-742 (1,1,3,3-tetramethyl-1,3-disilacyclobutane) from Starfire Systems or TSCH (1,3,5-trisilacyclohexane) from Gelest Inc. were used as the silicon and carbon source. After the SiC or SiC:0 growth, anisotropic fluorine-based (combination of CHF3 and CF4 gases) reactive ion etch was performed using a Plasma-Therm Versalock 700 to remove the top SiC or SiC:0 layer, leaving the sidewall layers intact and exposing the HSQ ribbon template. A wet-etch using BHF acid was then carried out to remove the HSQ, yielding ultrathin NWs synthesized in a self-aligned manner.

5.2 Device modeling

The calculations of the extraction efficiency and the spatial distribution of the dipole radiation were carried out using 3D finite-difference time-domain (FDTD) simulations (Lumerical Inc.). A *y*-polarized single dipole source was positioned at the center of a uniform slab (thin-film) and of a NW-PC structure (Figure 2a). The spatial dimension of the simulation window was varied to keep the total number of NWs (21 pairs) the same for all structures. We used a fixed grid size of 1 nm, and a perfectly matched layer as the boundary condition in all directions [30]. We used a monitor (parallel to the *xy*-plane) to calculate the transmitted flux through the top surface of the slab. It consisted of one 2 μ m × 2 μ m *xy* plane at *z* = 500 nm from the surface of the material (Figure 2a).

The position and dimensions of the monitor were kept the same for all simulations to ensure equivalent solid angle detection. We then calculated the total power injected by the dipole ($P_{\rm in}$) by integrating the time averaged Poynting flux over the six surfaces of a cube enclosing the radiating dipole. The extracted power ($P_{\rm out}$) was calculated from the power transmitted through the monitor plane. The extraction efficiency $\eta_{\rm ext}$ is defined as the ratio of $P_{\rm out}$ / $P_{\rm in}$ [19,30]. The index of refraction n, thickness, and geometry values for the thin-film and NW-PC structures, used in the simulations, were experimentally determined by SEM and spectroscopic ultraviolet-visible ellipsometry measurements (J.A. Woollam RC2 dual rotating compensator ellipsometer).

5.3 PL characterization

A home-built micro-PL (µPL) system -composed of an argon laser (Beamlock 2065-7S) coupled to an FLSP920 spectrometer from Edinburgh Instruments, a Triax-550 spectrometer from Horiba Jobin Yvon and liquid nitrogen cooled Ge/ InGaAs detectors - was utilized for PL and power-dependence PL (PDPL) measurements. We performed the PL and PDPL measurements at room-temperature using 476 and 488 nm excitations, to optically excite the Er^{3+} ions, through a Zeiss 50x (NA = 0.85) objective lens. Time-resolved photoluminescence (TRPL) studies were conducted in the FLSP920 spectrometer utilizing a multi-channel scaling technique. An acousto-optic modulator (AOM) was used to create laser pulses with a ~500 μs FWHM, and 50 Hz repetition-rate for the NW-PC structures and 100 Hz for the thin-film. For PL measurements at 77K, a close-system cold-finger cryostat with Mitutoyo NIR 50× objective lens (NA = 0.55) was used in the same spectrometer. For the emissionpolarization anisotropy measurements, PL spectra were collected at different angle of a polarizer placed in front of the

tube lens.

Author Contributions

S.G. perceived the experiments; V.N., and N.T. carried out the nanofabrication and N.T., S.G and M.H. organized the ion implantation of the NW-PC nanostructures; N.T. and V.N. performed the FDTD calculations; N.T., V.K, and E.C conducted the structural characterization of the NW-PC and thin-film samples; N.T. and A.K performed the PL experiments and analyzed the experimental data; S.G and N.T wrote the main manuscript text.

Acknowledgements

This work was supported by the National Science Foundation

- [1] Kwiat, M.; Elnathan, R.; Pevzner, A.; Peretz, A.; Barak, B.; Peretz, H.; Ducobni, T.; Stein, D.; Mittelman, L.; Ashery, U.; Patolsky F. Highly Ordered Large-Scale Neuronal Networks of Individual Cells – Toward Single Cell to 3D Nanowire Intracellular Interfaces. ACS Appl. Mater. Interfaces 2012, 4, 3542–3549.
- [2] Koenderink, A. F.; Alu, A.; Polman, A. Nanophotonics: Shrinking Light-Based Technology. *Science* 2015, 348, 516–521.
- [3] Wu, R.; Zhou, K.; Yue, C. Y.; Wei, J.; Pan, Y. Recent Progress in Synthesis, Properties and Potential Applications of SiC Nanomaterials. *Prog. Mater. Sci.* **2015**, *72*, 1–60.
- [4] Peretz-Soroka, H.; Pevzner, A.; Davidi, G.; Naddaka, V.; Tirosh, R.; Flaxer, E.; Patolsky, F. Optically-Gated Self-Calibrating Nanosensors: Monitoring pH and Metabolic Activity of Living Cells. *Nano Lett.* 2013, 13, 3157–3168.
- [5] He, Y.; Fan, C.; Lee, S.-T. Silicon Nanostructures for Bioapplications. Nano Today 2010, 5, 282–295.
- [6] Peng, K.-Q.; Wang, X.; Li, L.; Hu, Y.; Lee, S.-T. Silicon Nanowires for Advanced Energy Conversion and Storage. *Nano Today* 2013, 8, 75– 97.
- [7] Priolo, F.; Gregorkiewicz, T.; Galli, M.; Krauss, T. F. Silicon Nanostructures for Photonics and Photovoltaics. *Nat. Nanotechnol.* 2014, 9, 19–32.
- [8] Babinec, T. M.; Hausmann, B. J. M.; Khan, M.; Zhang, Y.; Maze, J. R.; Hemmer, P. R.; Lončar, M. A Diamond Nanowire Single-Photon Source. *Nat. Nanotechnol.* 2010, 5, 195–199.
- [9] Lohrmann, A.; Johnson, B. C.; McCallum, J. C.; Castelletto, S. A Review on Single Photon Sources in Silicon Carbide. *Reports Prog. Phys.* 2017, 80, 34502.
- [10] Thiel, C. W.; Böttger, T.; Cone, R. L. Rare-Earth-Doped Materials for Applications in Quantum Information Storage and Signal Processing. *J. Lumin.* 2011, 131, 353–361.
- [11] Simon, C.; Afzelius, M.; Appel, J.; Boyer de la Giroday, A.; Dewhurst,
 S. J.; Gisin, N.; Hu, C. Y.; Jelezko, F.; Kröll, S.; Müller, J. H.; et al.
 Quantum Memories. Eur. Phys. J. D 2010, 58, 1–22.
- [12] Saglamyurek, E.; Jin, J.; Verma, V. B.; Shaw, M. D.; Marsili, F.; Nam, S. W.; Oblak, D.; Tittel, W. Quantum Storage of Entangled Telecom-Wavelength Photons in an Erbium-Doped Optical Fibre. *Nat. Photonics* 2015, 9, 83–87.
- [13] Zhong, T.; Kindem, J. M.; Bartholomew, J. G.; Rochman, J.; Craiciu, I.; Miyazono, E.; Bettinelli, M.; Cavalli, E.; Verma, V.; Nam, S. W.; Marsili, F.; Shaw, M. D.; Beyer, A. D.; Faraon, A. Nanophotonic Rare-Earth Quantum Memory with Optically Controlled Retrieval. *Science* 2017, 357, 1392–1395.

through grant No ECCS-1842350. This work was also supported by the College of Nanoscale Science and Engineering of SUNY Polytechnic Institute, and the Research Foundation for the State University of New York. Their support is gratefully acknowledged. Authors gratefully acknowledge engineer C. Johnson for the TEM sample preparation and B. Harrington for helping in conducting experiments during his undergraduate research (REU) project.

References

- [14] Aharonovich, I.; Toth, M. Silicon Carbide Goes Quantum. Nat. Phys. 2014, 10, 93–94.
- [15] Fuchs, F.; Stender, B.; Trupke, M.; Simin, D.; Pflaum, J.; Dyakonov, V.; Astakhov, G. V. Engineering near-Infrared Single-Photon Emitters with Optically Active Spins in Ultrapure Silicon Carbide. *Nat. Commun.* 2015, 6, 1–7.
- [16] Castelletto, S.; Johnson, B. C.; Zachreson, C.; Beke, D.; Balogh, I.; Ohshima, T.; Aharonovich, I.; Gali, A. Room Temperature Quantum Emission from Cubic Silicon Carbide Nanoparticles. ACS Nano 2014, 8, 7938–7947.
- [17] Böttger, T.; Thiel, C.W.; Sun, Y.; Cone, R.L. Optical decoherence and spectral diffusion at 1.5 m in Er3+:Y2SiO5 versus magnetic field, temperature, and Er3+ concentration. *Phys. Rev. B* 2006, 73, 075101.
- [18] Gallis, S.; Huang, M.; Kaloyeros, A. E. Efficient Energy Transfer from Silicon Oxycarbide Matrix to Er Ions via Indirect Excitation Mechanisms. Appl. Phys. Lett. 2007, 90, 161914.
- [19] Fan, S.; Villeneuve, P. R.; Joannopoulos, J. D.; Schubert, E. F. High Extraction Efficiency of Spontaneous Emission from Slabs of Photonic Crystals. *Phys. Rev. Lett.* 1997, 78, 3294–3297.
- [20] Noda, S.; Fujita, M.; Asano, T. Spontaneous-Emission Control by Photonic Crystals and Nanocavities. *Nat. Photonics* **2007**, *1*, 449–458.
- [21] Dibos, A. M., Raha, M., Phenicie, C. M., & Thompson, J. D. Atomic Source of Single Photons in the Telecom Band. *Phys. Rev. Lett.* 2018, 120, 243601.
- [22] Schmidt, V.; Gosele, U. Materials science: How nanowires grow. *Science* **2007**, *316*, 698–699.
- [23] Kwiat, M.; Cohen, S.; Pevzner, A.; Patolsky, F. Large-scale ordered 1D-nanomaterials arrays: Assembly or not? *Nano Today* **2013**, 8, 677–694.
- [24] Nikas, V.; Tabassum, N.; Ford, B.; Smith, L.; Kaloyeros, A. E.; Gallis, S. Strong Visible Light Emission from Silicon-Oxycarbide Nanowire Arrays Prepared by Electron Beam Lithography and Reactive Ion Etching. J. Mater. Res. 2015, 30, 3692–3699.
- [25] Tabassum N., Kotha M., Kaushik V., Ford B., Dey S., Crawford E., Nikas V., and Gallis S. On-demand CMOS-Compatible Fabrication of Ultrathin Self-Aligned SiC Nanowire Arrays. *Nanomaterials* 2018, 8, 906.
- [26] Tabassum, N.; Nikas, V.; Ford, B.; Huang, M.; Kaloyeros, A. E.; Gallis, S. Time-Resolved Analysis of the White Photoluminescence from Chemically Synthesized SiC_xO_y Thin Films and Nanowires. *Appl. Phys. Lett.* 2016, 109, 43104.

- [27] Ford, B.; Tabassum, N.; Nikas, V.; Gallis, S. Strong Photoluminescence Enhancement of Silicon Oxycarbide through Defect Engineering. *Materials*. 2017, 10, 446.
- [28] Pacheco, J. L., Singh, M., Perry, D. L., Wendt, J. R., Ten Eyck, G., Manginell, R. P., ... & Bielejec, E. (2017). Ion implantation for deterministic single atom devices. *Review of Scientific Instruments*, 88(12), 123301.
- [29] Shinada, T.; Okamoto, S.; Kobayashi, T.; Ohdomari, I. Enhancing semiconductor device performance using ordered dopant arrays. Nature 2005, 437, 1128–1131
- [30] Fujita, M.; Takahashi, S.; Asano, T.; Tanaka, Y.; Kounoike, K.; Yamaguchi, M.; Nakanishi, J.; Stumpf, W.; Noda, S. Controlled Spontaneous-Emission Phenomena in Semiconductor Slabs with a Two-Dimensional Photonic Bandgap. J. Opt. A Pure Appl. Opt. 2006, 8, S131–S138.
- [31] Gallis, S.; Nikas, V.; Huang, M.; Eisenbraun, E.; Kaloyeros, A. E. Comparative Study of the Effects of Thermal Treatment on the Optical Properties of Hydrogenated Amorphous Silicon-Oxycarbide. *J. Appl. Phys.* 2007, 102.
- [32] Madapura, S. Heteroepitaxial Growth of SiC on Si (100) and (111) by Chemical Vapor Deposition Using Trimethylsilane. *J. Electrochem.* Soc. 1999, 146, 1197–1202.
- [33] W. J. Miniscalo, J. Lightwave Technol. 9, 234 (1991).
- [34] A.J. Kenyon. "Recent developments in rare-earth doped materials for optoelectronics". Progress in Quantum Electronics 26, 225 (2002).
- [35] Kurtsiefer, C.; Mayer, S.; Zarda, P.; Weinfurter, H. Stable Solid-State Source of Single Photons. *Phys. Rev. Lett.* 2000, 85, 290–293.
- [36] Elliman, R. G.; Wilkinson, A. R.; Kim, T.-H.; Sekhar, P. K.; Bhansali, S. Optical Emission from Erbium-Doped Silica Nanowires. *J. Appl. Phys.* 2008, 103, 104304.
- [37] Sardar, D. K.; Russell III, C. C.; Gruber, J. B.; Allik, T. H; Absorption intensities and emission cross sections of principal intermanifold and inter-Stark transitions of Er³⁺(⁴f₁₁) in polycrystalline ceramic garnet Y₃Al₅O₁₂. J. Appl. Phys. 2005, 97, 123501.
- [38] Suh, K.; Lee, M.; Chang, J. S.; Lee, H.; Park, N.; Sung, G. Y.; Shin, J. H.; Cooperative upconversion and optical gain in ion-beam sputter-deposited Er_xY_{2-x}SiO₅ waveguides. *Opt. Exp.*, 2010, 18, 7724.

- [39] Ruda, H. E., & Shik, A.; Polarization-sensitive optical phenomena in semiconducting and metallic nanowires. *Phy. Rev. B*, **2005**, *72*, 115308.
- [40] Rivas, J. G.; Muskens, O. L.; Borgström, M. T.; Diedenhofen, S. L.; Bakkers, E. P.A.M. Optical Anisotropy of Semiconductor Nanowires. In *One-Dimensional Nanostructures*. Wang, Z. M.; Springer: New York, 2008; pp 127-145.
- [41] Wang, Zhiming M., ed. One-dimensional nanostructures. Vol. 3. Springer Science & Business Media, 2008.
- [42] Inam, F. A.; Grogan, M. D. W.; Rollings, M.; Gaebel, T.; Say, J. M.; Bradac, C.; Birks, T. A.; Wadsworth, W. J.; Castelletto, S.; Rabeau, J. R.; et al. Emission and Nonradiative Decay of Nanodiamond NV Centers in a Low Refractive Index Environment. ACS Nano 2013, 7, 3833–3843.
- [43] Vinh, N. Q.; Minissale, S.; Vrielinck, H.; Gregorkiewicz, T. Concentration of Er³⁺ Ions Contributing to 1.5-μm Emission in Si/Si:Er Nanolayers. *Phys. Rev. B* 2007, 76, 85339.
- [44] Liu, G. K.; Zhuang, H. Z.; Chen, X. Y. Restricted Phonon Relaxation and Anomalous Thermalization of Rare Earth Ions in Nanocrystals. *Nano Lett.* **2002**, *2*, 535–539.
- [45] Estes, M. J.; Moddel, G. Luminescence from Amorphous Silicon Nanostructures. *Phys. Rev. B* **1996**, *54*, 14633–14642.
- [46] Thillosen, N.; Sebald, K.; Hardtdegen, H.; Meijers, R.; Calarco, R.; Montanari, S.; Kaluza, N.; Gutowski, J.; Lüth, H. The State of Strain in Single GaN Nanocolumns as Derived from Micro-Photoluminescence Measurements. *Nano Lett.* 2006, 6, 704-708.
- [47] Thelander, C.; Agarwal, P.; Brongersma, S.; Eymery J.; Feiner, L.; Forchel, A.; Scheffler, M.; *et al.* Nanowire-based One-Dimensional Electronics. *Materials Today* **2006**, *9*, 28-35.
- [48] R. Li, S. Yerci, and L. Dal Negro. "Temperature dependence of the energy transfer from amorphous silicon nitride to Er ions". Appl. Phys. Lett. 95, 041111 (2009).
- [49] A.J. Kenyon. "Recent developments in rare-earth doped materials for optoelectronics". Progress in Quantum Electronics 26, 225 (2002).

Supplementary Material

Engineered Telecom Emission and Controlled Positioning of Er³⁺ Enabled by SiC Nanophotonic Structures

Natasha Tabassum,¹ Vasileios Nikas,¹ Alex E. Kaloyeros,¹ Vidya Kaushik,¹ Edward Crawford,² Mengbing Huang,¹ and Spyros Gallis¹ (🖂)

² GLOBALFOUNDRIES Corp., East Fishkill, New York 12533, USA

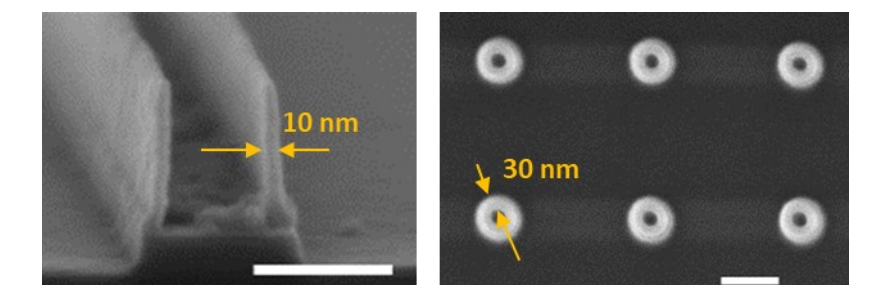


Figure S1: (left) High magnification cross-section SEM images of the resulting NW-PC structures with W= 10 nm. (right) Top-down SEM of arrays of nanotubes, fabricated with similar integration steps as figure 1. Scale bars at both images are 100 nm.

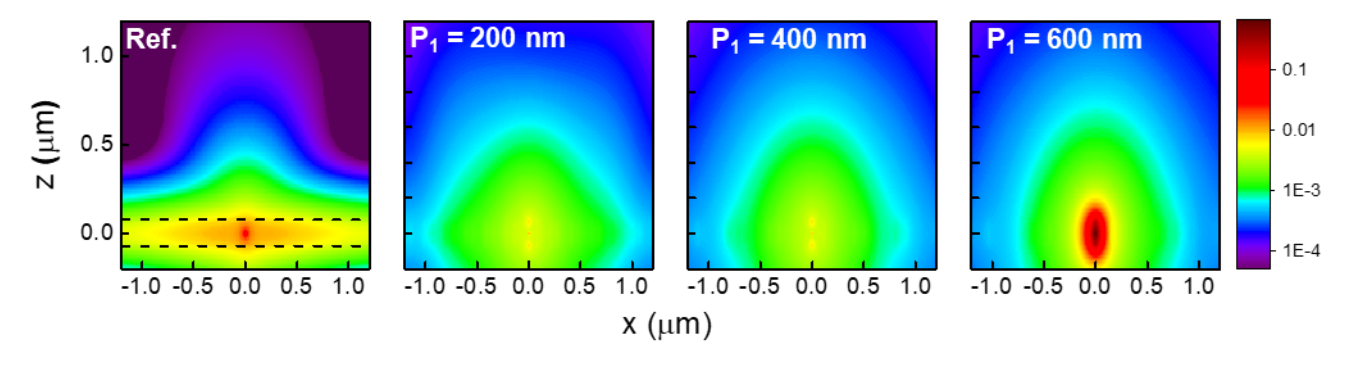


Figure S2: Calculated spatial distribution of $|E|^2$ at 1540 nm in the zx plane (y-polarized dipole, n = 2.7) for the reference thin-film (dashed lines represent the outline of the film), the 200-nm-P₁ , 400-nm-P₁ and the 600-nm-P₁ NW-PC.

¹ College of Nanoscale Science and Engineering, SUNY Polytechnic Institute (SUNY Poly), Albany, New York 12203, USA

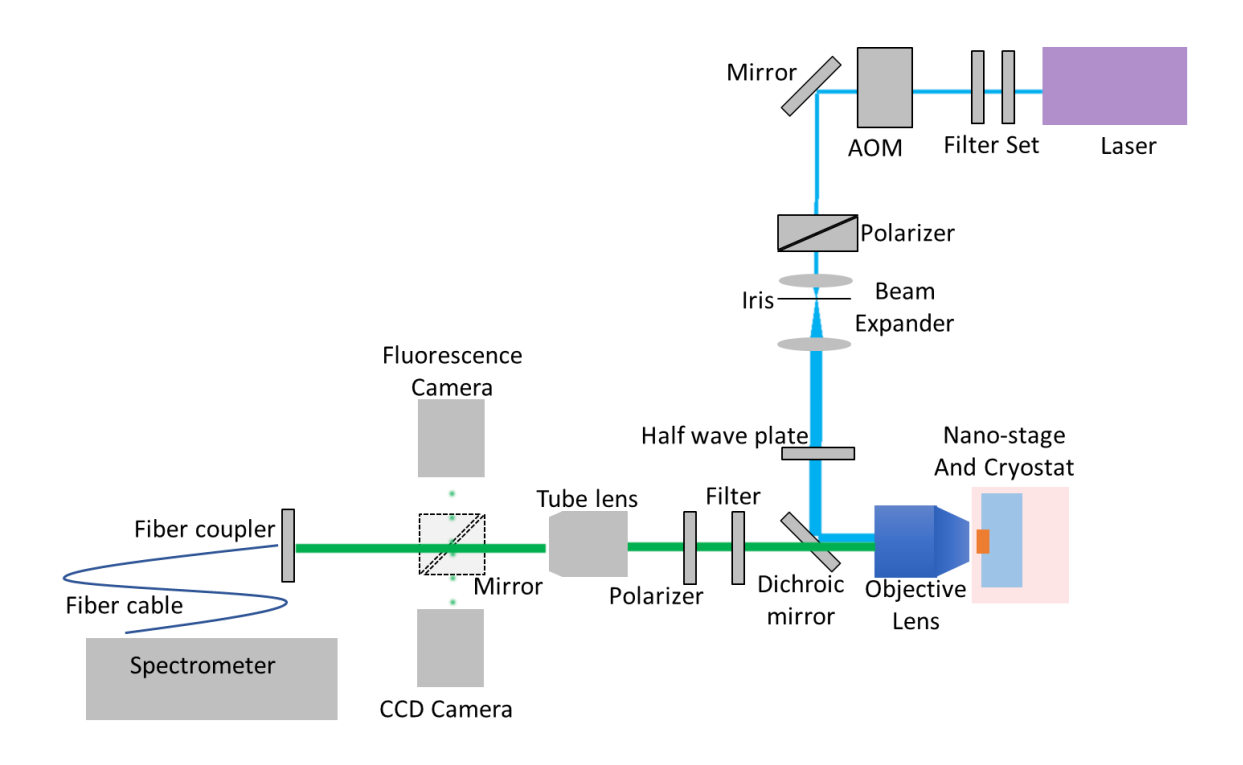


Figure S3: Schematic diagram of the micro-photoluminescence spectrometer used to study the emission properties of erbium ions in NW-PC and thin-film samples. [AOM: acousto-optic modulator, CCD: Charge-Coupled Device]

S4: Visible emission (~550 nm) in NW-PC

As expected, due to their volumetric difference, visible PL of NW-PC from multiple different structures showed a steady decrease in PL intensity with larger periodicity P_1 (Figure 3b). PL intensity at 550 nm is plotted in Figure 4a as a function of P_1 in NW-PC. After normalizing the PL intensities with the corresponding volume differences (Section S5), the PL intensity of each structure became close in value within 10% variation, as shown in Figure S4-a. This behavior suggests that the PL intensity difference is mainly dominated by the difference in the excited volume of the material. Average lifetime at 550 nm was found to be \sim 680 \pm 40 ps from all four structures (Figure S4-b).

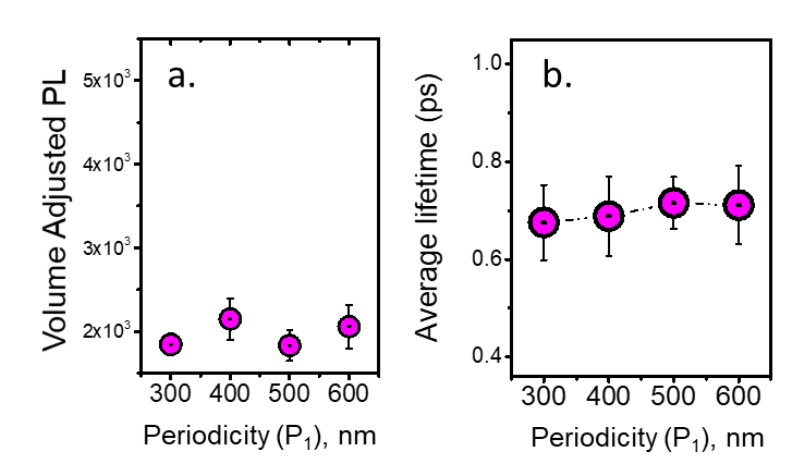


Figure S4: (a) Visible PL from NWs after the volumetric adjustment. (b) Average lifetime of each structure.

S5: Volumetric difference between nanostructures

Under the same excitation laser beam-diameter, the actual volume of excited material varies for different nanowire array structures. For example, nanowire arrays with larger periodicity P_1 result in the excitation beam-diameter falling on a lesser number of nanowires, and therefore less volume. The relative volumetric difference for the studied nanowire-based photonic crystal structures (NW-PC) are shown in Figure S5.

To this end, the difference of implanted Er ions was accounted for among the different NW-PC structures and also between the NW-PC and thin-film (decrease in the number of Er^{3+} ions in the air region with increasing P_1) when plotting the Er^{3+} PL intensity.¹ Considering the effective area-difference between the thin-film and NW-PC we have: x-direction, 1000 nm (film) / 80 nm (corresponds to 4 NWs in the 600-nm- P_1 structure) = 12; and y-direction, no difference. Therefore, to compare the Er^{3+} PL spectra between the 600-nm- P_1 NW-PC and thin-film, we divided the PL intensity in thin-film with 12.

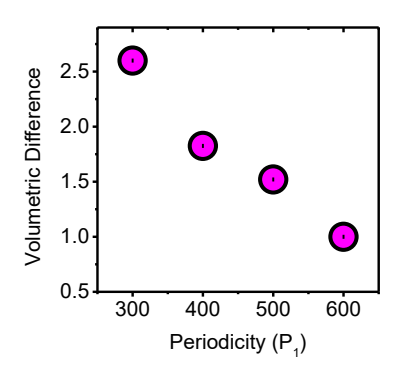


Figure S5: Relative difference in the volume of excited material for the studied NW-PC structures with periodicity from 300 nm to 600 nm (P1) under the same excitation beam-diameter.

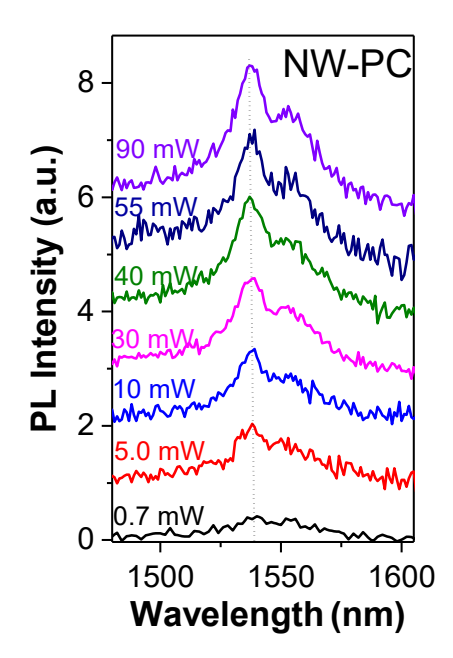


Figure S6: Room-temperature Er³⁺ emission spectra of the 600-nm-P₁ NW-PC under different pumping powers of 488 nm excitation.

S7: Estimation of the optically active Er ion concentration

The estimation of the optically active Er^{3+} concentration ratio, N^* , between the NW-PC and reference thin-film was carried out by using equation (5). First, we calculated the ratio of the radiative lifetimes between the NW-PC structure $(\tau_{r,NW} = \Gamma_{r,NW}^{-1})$ and reference $(\tau_{r,ref} = \Gamma_{r,ref}^{-1})$ using 3D FDTD simulation. The total power P radiated by a dipole is determined by the photon density of states (DOS) in the emitter-environment system and is proportional to the radiative spontaneous emission rate. As described in the device modeling section, the total radiated power in the NW-PC structure with n = 2.2 (SiC:O) was calculated from the power transmitted through a cube enclosing the radiating dipole. An average radiated power, $P_{\rm NW}$ of all three directional dipoles was used for this calculation. Similarly, $P_{\rm ref}$ was calculated for the same dipole orientations in the slab (n = 2.2). The ratio of the radiative spontaneous emission rates between the NW-PC and reference was then calculated as $\frac{P_{\rm NW}}{P_{\rm ref}} = \frac{\Gamma_{\rm r,NW}}{\Gamma_{\rm r,ref}}$. Considering the ratio of their FDTD-simulated

extraction efficiencies $(\frac{n_{ext. ref}}{n_{ext. NW}} \approx 0.22)$, we then calculated N^* of the NW-PC relative to reference from Eq. (5) as

$$\frac{N_{NW}^*}{N_{ref}^*} = \frac{n_{ext.\ ref}}{n_{ext.\ NW}} \times \frac{I_{sat,NW}}{I_{sat,ref}} \times \frac{\tau_{r,NW}}{\tau_{r,ref}} \approx 0.22 \times 22 \times 2.56 \approx 12.4$$

We also accessed the ratio of emission rates by employing the analytical expression for the emission transition rate of a dipole inside high-index nanoparticle emitting in air.^{4,5} In this case, Γ_r , which is considered independent of the position of the dipole and the polarization in the nanoparticle, is smaller compared to the rate in bulk and can be approximated by $\frac{\Gamma_{r,NW}}{\Gamma_{r,ref}} = 9/n(n^2 + 2)^2$.

However, this relation considers dipoles inside a spherical dielectric nanoparticle. In this respect, this result can be only considered as an approximate upper limit for the change in the spontaneous emission rate of a dipole in SiC:O NWs, and thus was not used in determining N^* .

S8: Er3+ PL dynamics of the thin-films

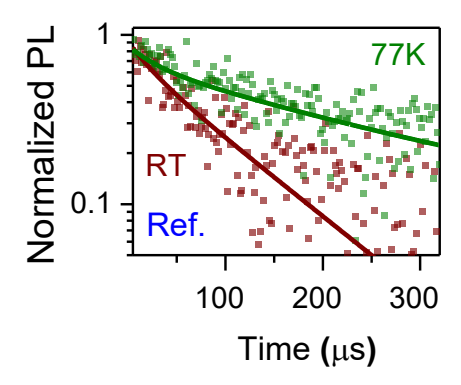


Figure S8: The average Er^{3+} PL lifetime was $110 \pm 10 \mu s$ (RT: 300 K) and $280 \pm 20 \mu s$ (77 K) as calculated from the integrated luminescence decays [25]. The solid lines indicate fits to the data.

¹ Fan, S.; Villeneuve, P. R.; Joannopoulos, J. D.; Schubert, E. F. High Extraction Efficiency of Spontaneous Emission from Slabs of Photonic Crystals. *Phys. Rev. Lett.* **1997**, *78*, 3294–3297.

² Fujita, M.; Takahashi, S.; Asano, T.; Tanaka, Y.; Kounoike, K.; Yamaguchi, M.; Nakanishi, J.; Stumpf, W.; Noda, S. Controlled Spontaneous-Emission Phenomena in Semiconductor Slabs with a Two-Dimensional Photonic Bandgap. *J. Opt. A Pure Appl. Opt.* **2006**, *8*, S131–S138.

³ Inam, F. A.; Grogan, M. D. W.; Rollings, M.; Gaebel, T.; Say, J. M.; Bradac, C.; Birks, T. A.; Wadsworth, W. J.; Castelletto, S.; Rabeau, J. R.; et al. Emission and Nonradiative Decay of Nanodiamond NV Centers in a Low Refractive Index Environment. ACS Nano 2013, 7, 3833–3843.

⁴ Chew, H. Radiation and lifetimes of atoms inside dielectric particles. *Phys. Rev. A*, **1988**, 38, 3410–3416.

⁵ Schuurmans, F. J. P.; De Lang, D. T. N.; Wegdam, G. H.; Sprik, R.; Lagendijk, A. Local-Field Effects on Spontaneous Emission in a Dense Supercritical Gas. *Phys. Rev. Lett.* **1998**, 80 (23), 5077–5080.